**Supplemental Material**

# Atomic Scale Control of Plasmon Modes in Gaphene Nanoribbons

François Aguillon,[1] Dana Codruta Marinica,[1] and Andrei G. Borisov[1,*]

[1] *Institut des Sciences Moléculaires d'Orsay (ISMO), UMR 8214, CNRS, Université Paris-Saclay, bât 520, Orsay Cedex, France*

(Dated: October 24, 2021)

## Abstract

In this Supplemental Material we provide

- Brief description of the time-dependent tight-binding approach.
- Discussion of the robust character of the results with respect to the plasmon mode broadening because of the coupling to optical phonons.
- Analysis of the evolution of the plasmon modes for the separated nanoribbon dimer upon the closing of the dimer gap.
- The electronic band structure of the infinite AGNR-11 and ZGNR-12 nanoribbons.
- The dependence of the optical response of the nanoribbon on the transversal displacement of the vacancy (the effect of the choice of the carbon atom row) and on the electronic doping given by the Fermi energy.
- Analysis of the transition to the wide ribbon limit.


## TIME-DEPENDENT TIGHT-BINDING METHOD

Atomic units are used in this section unless otherwise stated.

### The time-dependent equation

The time-dependent tight-binding (TDTB) method describing the electron density dynamics in response to an external potential acting on graphene nanostructures has been described in great details elsewhere [1]. Here we give only the brief summary of this technique developed on the basis of the random phase approximation [2] and, later, density matrix approaches [3] successfully applied to address plasmonic excitations in graphene nanoflakes and nanoribbons [2–6]. Thus, the time-dependent wave functions of the occupied orbitals $\Psi_j(\mathbf{r},t)$ of graphene nanstructure are represented in the basis of the carbon atom $2p$-orbitals, $\psi_{2p}(\mathbf{r}-\mathbf{r}_\ell)$, centered on the lattice sites $\mathbf{r}_\ell$ of the nanoribbon.

$$\Psi_j(\mathbf{r},t) = \sum_\ell C_\ell(j,t)\ \psi_{2p}(\mathbf{r}-\mathbf{r}_\ell), \tag{S1}$$

where index $j = 1, \ldots, j_{max}$ enumerates the occupied orbitals of the ground state system, and $\ell = 1, \ldots, \mathcal{N}$. Here, $\mathcal{N}$ is the number of the carbon atoms in the nanostructure.

The tight binding representation given by Eq. S1 results in the non-linear Scrödinger equation

$$i\partial_t \mathbb{C}(j,t) = \mathbb{H}[q](t)\ \mathbb{C}(j,t) \tag{S2}$$

for the time-evolution of the vector $\mathbb{C}(j,t)$ given by the column of the $C_\ell(j,t)$ coefficients. The initial conditions $\mathbb{C}(j, t = 0)$ are given by the occupied orbitals of the ground-state system. The off-diagonal elements of the tight-binding Hamiltonian matrix $\mathbb{H}[q](t)$ are given by $\mathbb{H}_{\ell\ell'}(t) = -t$, where indexes $\ell$ and $\ell'$ denote the nearest neighbours, and $t = 2.7$ eV is the hopping integral. The diagonal elements express the total potential at the carbon lattice site $\ell$

$$\mathbb{H}_{\ell\ell}(t) = V_{ext}(\mathbf{r}_\ell, t) + \sum_{\ell' \neq \ell} \frac{q_{\ell'}}{|\mathbf{r}_\ell - \mathbf{r}_{\ell'}|} + v_{\ell\ell} q_\ell. \tag{S3}$$

In Eq. S3 the first term is given by an external potential, the second term expresses potential owing to the charges, $q_{\ell'}$, induced at the $\ell'$ lattice sites $q_{\ell'} = \sum_j \left[|C_{\ell'}(j,t)|^2 - |C_{\ell'}(j,t=0)|^2\right]$, and the last term stands for the onsite Hubbard interaction with $v_{\ell\ell} = 0.58$ [2]. Since the size of the system under the study is essentially smaller than the relevant wavelength of the electromagnetic radiation, we use the non-retarded approximation for potentials.

The vacancy at the lattice site $\ell_v$ is introduced by setting to zero the $\mathbb{H}_{\ell\ell_v}(t)$ matrix elements of the Hamiltonian for $(\ell = 1, ..., \mathcal{N})$. We also define the vacancy positions with longitudinal coordinate $x_v$ and the number of carbon atom row, $N_v$, at which the vacancy is created, where $1 \leq N_v \leq N$, and $N$ is the total number of carbon atom rows forming the nanoribbon (see Fig. 1 of the main text).

Equations S2 are solved using the short time-step $\Delta t$ propagation based on the Lanczos technique [7]. Typically $\Delta t = 1$ a.u. From the time-dependent induced charges $q_{\ell'}(t)$ one obtains the dipole $\mathbf{P}(t)$ or higher-order multipole moments of graphene nanostructure, as well as the induced current $I_{\rm ind}(t,x)$, and the induced electric field $\mathbf{E}^{\rm ind}(t,\mathbf{r})$ created by graphene nanostructure in response to an external potential. The induced current through the transversal cross-section of the nanoribbon can be obtained from continuity equation considering variation of charge within the $[x, x + \Delta x]$ section of the nanoribbon (obviously, within the TDTB approach, the $x$-coordinate takes the discrete values).

The frequency-resolved quantities are obtained using the time-to-frequency Fourier trans-

form. E.g. for the induced dipole

$$\mathbf{P}(\omega) = \int_0^T \mathbf{P}(t)\ e^{i(\omega+i\gamma)t}\ \mathrm{d}t, \tag{S4}$$

where $T$ is the finite albeit large propagation time. Similarly, for the induced current characterising the plasmon mode $p$

$$I_{\mathrm{ind}}(p,x) = \int_0^T I_{\mathrm{ind}}(t,x)\ e^{i(\omega_p+i\gamma)t}\ \mathrm{d}t, \tag{S5}$$

where $\omega_p$ is the plasmon mode frequency. In Eqs. S4 and Eqs. S5, parameter $\gamma$ introduces an artificial broadening of the spectral features allowing to phenomenologically account for the broadening effects beyond the TDTB description. This is the case for the plasmon decay with optical phonon excitation discussed below.

**Excitation**

The optical response and plasmon modes of graphene nanoribbons (GNRs) are studied using the plane wave and point dipole excitation (see the main text for the definition of the geometry of the system).

Thus, to calculate the response on the excitation with the electromagnetic $x$-polarized plane wave we use the impulsive perturbation with an electric field along the nanoribbon $x$-axis $E(t) = E_0\ \delta(t)$ so that $V_{ext}(\mathbf{r}_\ell, t) = E_0\ x_\ell\ \delta(t)$. Here $x_\ell$ is the projection of the position vector $\mathbf{r}_\ell$ of the carbon lattice site on the $x$-axis. The absorption cross-section is then obtained from

$$\sigma(\omega) = \frac{4\pi\omega}{cE_0}\ \mathrm{Im}\left\{P_x(\omega)\right\}, \tag{S6}$$

where $P_x$ is the $x$-component of the induced dipole $\mathbf{P}(\omega)$, $\mathrm{Im}\left\{Z\right\}$ stands for the imaginary part of a complex number $Z$, and $c$ is the speed of light in vacuum. As discussed in the main text, analysis of $\sigma(\omega)$ reveals the effect of the carbon atom vacancy on the optical absorption and, via the resonant features in $\sigma(\omega)$, on the dipolar plasmon of the nanoribbon.

The excitation of the nanoribbon with a quantum emitter (QE) allows to visualise the vacancy effect not only on the dipolar plasmon, but also on the higher order dark and bright plasmon modes. To this end we use an impulsive dipole perturbation $d(t) = d_0\delta(t)$ where $d(t)$ is the $x$-oriented point dipole located at $\mathbf{r}_d$. In this situation, the external potential

$$V_{ext}(\mathbf{r}_\ell, t) = d_0\ v_{\mathrm{dip}}\left(\mathbf{r}_\ell - \mathbf{r}_d\right)\ \delta(t), \tag{S7}$$

where

$$v_{\mathrm{dip}}\left(\mathbf{r}_\ell - \mathbf{r}_d\right) = \frac{\hat{e}_x \cdot \left(\mathbf{r}_\ell - \mathbf{r}_d\right)}{\left|\mathbf{r}_\ell - \mathbf{r}_d\right|^3}. \tag{S8}$$

Here $\hat{e}_x$ is the unit length vector alon $x$-axis.

The field induced by the nanostructure $\mathbf{E}^{\mathrm{ind}}(\omega, \mathbf{r})$ in response to the point dipole excitation allows one to calculate the tensor components of $\mathbf{G}_{ns}$, where $\mathbf{G}_{ns}$ is the change of the free-space Green's tensor because of the presence of the nanostructure. Thus

$$G_{ns}(\mathbf{r}, \mathbf{r}_d)_{jx} = \left[\frac{4\pi}{c^2}\omega^2 d_0\right]^{-1} \hat{e}_j \cdot \mathbf{E}^{\mathrm{ind}}(\omega, \mathbf{r}), \tag{S9}$$

where $(j = x, y, z)$. Since the imaginary part of the Green's tensor is related to photonic density of states [8], it reveals the bright and the dark plasmon modes of the nanoribbon.

Nevertheless, we prefer to discuss in the main text of the paper the Purcell factor $\mathcal{F}$ which characterizes the decay rate of a quantum emitter in plasmonic environment. Thus, the TDTB results for $\mathcal{F}$ illustrate the possibility to tune the decay rate of a quantum emitter by selecting position of a single carbon atom vacancy within the nanoribbon. The transition frequency $\omega$-dependent Purcell factor is obtained from [9]

$$\mathcal{F} = \frac{\Gamma}{\Gamma_{\mathrm{v}}} = 1 + \frac{6\pi c}{\omega}\, \mathrm{Im}\left\{\hat{e}_x \mathbf{G}_{ns}(\mathbf{r}_d, \mathbf{r}_d)\hat{e}_x\right\}, \tag{S10}$$

where $\Gamma$ is the decay rate of a QE in presence of GNR, and $\Gamma_{\mathrm{v}}$ is the decay rate of a QE in vacuum. Using Eq. S9 one obtains

$$\mathcal{F} = 1 + \frac{3}{2d_0}\frac{c^3}{\omega^3}\, \mathrm{Im}\left\{E^{\mathrm{ind}}(\mathbf{r}_d)\right\}, \tag{S11}$$

where $E^{\mathrm{ind}}(\mathbf{r}_d)$ is the $x$-component of the electric field of graphene nanoribbon induced at position of the QE in response to the $x$-oriented point dipole located at the same position, and oscillating at the QE transition frequency $\omega$. Since the size of the studied system is much smaller than the relevant wavelength of electromagnetic radiation, the Purcell factor is determined by the nonradiative decay of the QE because of the interaction with GNRs [8–10]. This process is well described by our nonretarded calculations. The excitation of the plasmon modes in GNRs leads to the resonant features in the dependence of $\mathcal{F}$ on $\omega$ which allows their energy and lifetime analysis.

## EFFECT OF THE PLASMON DECAY OWING TO THE OPTICAL PHONON EXCITATION

For the realistic graphene nanoribbon several factors lead to the broadening of plasmon resonances. The TDTB approach includes the effect of the plasmon decay and dephasing owing to the Landau damping by scattering on the edges of the nanostructure or on the defects of graphene lattice [11–17]. However, the interaction with the substrate and optical phonons [11, 12, 18, 19] can induce further plasmon decay channels which are beyond the present TDTB description. The phenomenological account of these effects consists in introducing an artificial broadening $\gamma$ of the calculated frequency-dependent results (see Eq. (S4)).

In the main text of the paper, for the sake of the presentation we used relatively small $\gamma = 5$ meV. This allows to observe the sharp features in the calculated optical response owing to the excitation of the plasmon resonances of the nanoribbons. Consequently, the effects of the carbon atom vacancy at the focus of our work appear crystal clear, simplifying the discussion. This said, for the energies of the plasmon modes above the optical phonon frequency, $\approx 0.2$ eV, the plasmon decay with excitation of the optical phonons in graphene leads to an appreciable reduction of the plasmon lifetime [11, 12, 18, 19]. The associated plasmon line broadening can be estimated to be within $15 - 60$ meV range for the plasmon modes with frequencies $\omega \sim 0.5$ eV [19].

We have thus computed the data presented in Fig. 2 and in Fig. 4 of the main text introducing a broadening $\gamma = 30$ meV. As follows from the results presented in Fig. S1 and in Fig. S2 and their comparison with Fig. 2 and in Fig. 4 of the main text, the consequences of the presence of the vacancy defect – the blue shift of the bright plasmon modes for the AGNR-11, and their broadening and quenching for ZGNR-12 – remain clearly visible. Indeed, at least for the low energy plasmon modes, the energy shift and the broadening resulting from the presence of the carbon atom vacancy are essentially larger than 30 meV. This demonstrates the robust character of our results and conclusions with respect to the plasmon line broadening via different decay mechanisms, and, in particular, optical phonon excitation.

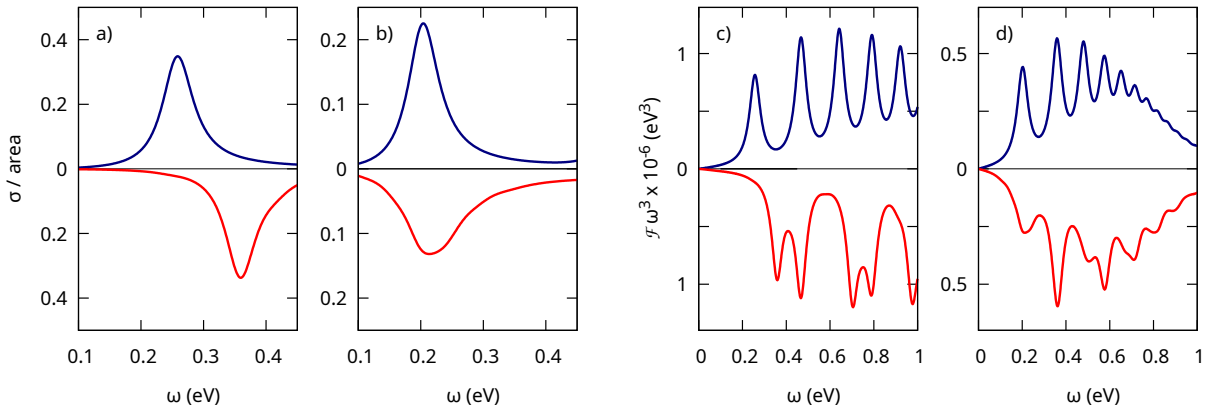


FIG. S1. Optical response of the AGNR-11 (panels **a,c**), and ZGNR-12 (panels **b,d**). The ZGNR-12 is electronically doped to Fermi energy $E_F$=0.4 eV, while the AGNR-11 is neutral ($E_F$=0). The Fermi energy is measured with respect to the Dirac point. The blue curves correspond to the ideal GNRs. The red curves correspond to defective GNRs with the single carbon atom vacancy at $x_v = 0.07$ nm, $N_v = 5$ (AGNR-11), and at $x_v = 0.12$ nm, $N_v = 6$ (ZGNR-12). **a, b**: The optical absorption cross section $\sigma$ of the GNRs normalized to their area. Results are shown as function of the frequency of the incident electromagnetic plane wave. **c, d**: The decay rate enhancement $\mathcal{F} \times \omega^3$ for the QE with transition frequency $\omega$ located in vicinity of GNRs at $x_d = h - L/2$ and $y_d = W/2$ as indicated in Fig. 1 of the main text. We use $h = 1$ nm. An artificial broadening $\gamma = 30$ meV has been applied.

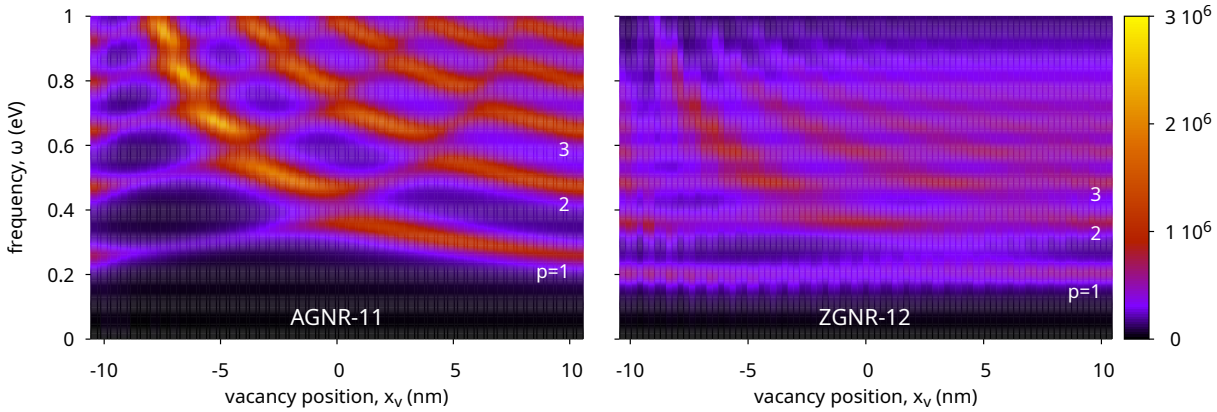


FIG. S2. The same as Fig. 4 of the main text, however for an artificial broadening $\gamma = 30$ meV.

## ANALYSIS OF THE EVOLUTION OF THE PLASMON MODES OF THE NANORIBBON DIMER UPON CLOSING OF THE DIMER GAP.

In the main text of the paper we have shown that the vacancy placed at the $N_v = 5$ atomic row at the middle of the AGNR-11 at $x_v \approx 0$ blueshifts the energy of the bright plasmon modes. This effect is attributed to the strong reflection of the electrons propagating along the nanoribbon by the carbon atom vacancy. The two parts of the nanoribbon at opposite sites of the vacancy region appear decoupled electronically. As a consequence, the $L$-long AGNR-11 responds to an optical excitation as a dimer of the $L/2$-long nanoribbons.

In Fig. S3, we further analyse the transformation of the coupled $L/2$ dimer with nonconductive junction into the single $L$-long nanoribbon, and we trace the corresponding evolution of the plasmon resonances. As sketched in the panels a-e zooming at the vacancy region, we start with single $L/2$-long AGNR-11 and progressively approach the second $L/2$-long AGNR-11 (panel b) up to the separation of 0.142 nm corresponding to the $L$-long nanoribbon, where the C-C bonds are broken along the transversal direction (panel c). Then, the $L$-long AGNR-11 with the vacancy defect (panel d) and an ideal $L$-long AGNR-11 (panel e) are considered.

For the $L/2$ AGNR-11 dimer the bonding and antibonding plasmon modes are formed from the plasmon modes of the individual $L/2$ - long nanoribbons [4, 20, 21]. Upon reducing the size of the junction of the dimer, its bonding modes are red shifting in energy and finally transform into to the bright plasmon modes of the $L$-long nanoribbon. The calculated here strong red-shift of the plasmon modes upon closing the gap is inline with previous calculations of the transverse plasmons in wide GNRs [4]. The transformation from the capacitively coupled dimer with accumulation of the induced charges of opposite sign across the gap to fully established conductive contact forming the $L$-long nanoribbon operates at the single atom level. Indeed, consider the evolution of the plasmon modes upon the c $\rightarrow$ d $\rightarrow$ e geometry transformation. The difference in the bonding plasmon mode energies obtained with broken C-C bonds (see Fig. S3c) and with single carbon atom vacancy (see Fig. S3d) might be related to the fact that the induced current near $x = 0$ is strictly zero in the former case, but it is finite in the later case (see Fig. 3 of the main text). In other words, the reflection induced by the vacancy creates a phase shift and slightly changes the energy of the standing plasmonic wave in the $L/2$ AGNR-11 resonator [22]. Removing the vacancy

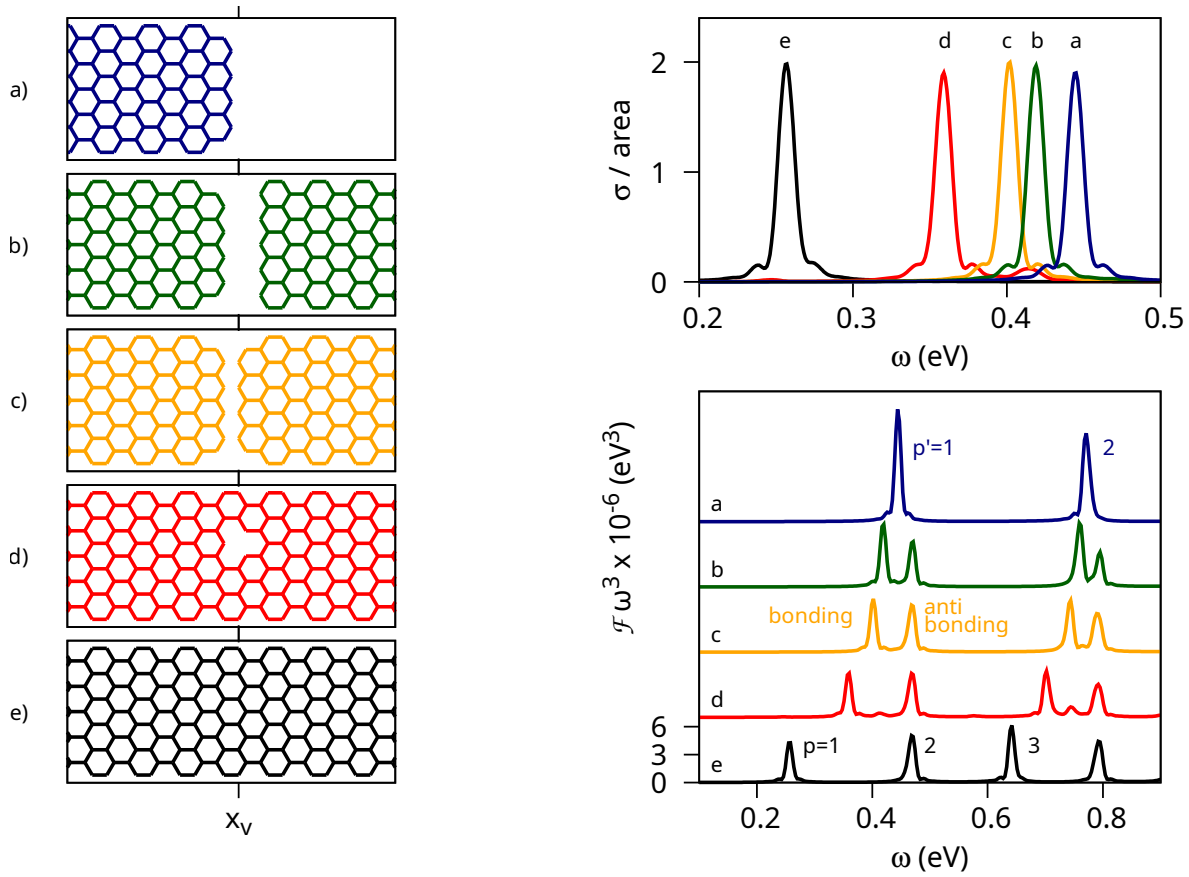


FIG. S3. **Left panels** Zoom into the gap geometries of ANGR-11 nanoribbons. **a:** an individual $L/2$-long nanoribbon; **b:** the dimer of the $L/2$ nanoribbons separated by the gap of 0.355 nm i.e. 2.5× the C-C bond length; **c:** idem with gap of 0.142 nm i.e. the C-C bond length; **d:** an $L$-long ANGR-11 with a vacancy; **e:** idem with no vacancy. The vacancy is at the $N_v = 5$ carbon atom row at $x_v = 0.07$ nm indicated by the vertical tick. **Right panels** The optical response. **Top right:** An absorption cross section $\sigma$ normalized to the area of the nanoribbon(s). Results calculated with TDTB for different geometries are shown as function of the frequency of the incident $x$-polarized electromagnetic plane wave. The geometry is indicated with color and label of the curve. **Bottom right:** Waterfall plot of the decay rate enhancement given by $\mathcal{F} \times \omega^3$ for the QE with transition frequency $\omega$ located in vicinity of GNRs as explained in Fig. 1 of the main text. Results for different geometries are shown as function of the transition frequency. For an ideal $L/2$ ($L$) GNRs the resonances are labelled with their "quantum number" $p'$ ($p$) in order of increasing energy. An artifical broadening $\gamma = 5$ meV has been applied.

fuses the dimer and results in formation of the dipolar mode of the $L$-long nanoantenna. The redshift of the plasmon resonance resulting from this single atom manipulation is comparable to that calculated for the dimer evolution from an infinite gap width to the gap width given by the length of the C-C bond.

The antibonding modes of the dimer evolve into the dark plasmon modes of the $L$-long nanoribbon. This later case does not involve the transformation of the induced charge density or appearance of the induced currents across the junction, which explains an extremely small energy shift of the plasmon modes with closing the gap.

## ELECTRONIC STRUCTURE OF THE NANORIBBON

In Fig. S4 we show the band structure of the (metallic) AGNR-11, and ZGNR-12. The electronic bands are associated with an electron propagating along the nanoribbon and confined in transversal direction.

For metallic AGNR-11, the well defined plasmon modes are formed without necessity for the charge doping because the chirality of the electron wavefunctions propagating along the ribbon blocks the plasmon decay into electron-hole pairs [23, 24]. For the ZGNR-12, the charge doping is necessary for plasmonic response. It is worth noting that for the ZGNR the non-dispersive states at zero energy are the so-called edge states [25].

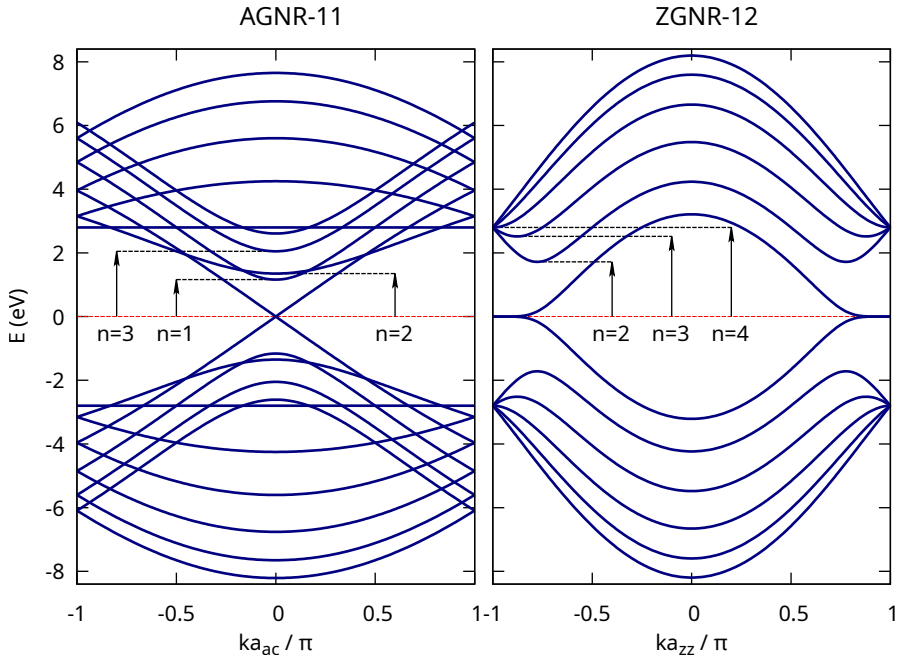


FIG. S4. The tight-binding electronic band structure of the metallic AGNR-11 and ZGNR-12 infinite in the longitudinal $x$-direction. The energies are measured with respect to the Dirac point. The longitudinal electron momentum is denoted by $k$. The nanoribbons are periodic along $x$ with period $a_{\rm ac} = 0.426$ nm ($a_{\rm zz} = 0.246$ nm) for armchair (zigzag) nanoribbons. The electronic bands at positive energies are labelled with their transversal quantum number $n$. The lowest energy band crossing the Dirac point corresponds to $n = 0$.

## ROLE OF THE TRANSVERSAL POSITION OF THE VACANCY AND OF THE CHARGE DOPING

In Fig. S5 we show the absorption cross-section calculated with TDTB for an electromagnetic $x$-polarised plane wave incident on defective nanoribbons. The carbon atom vacancy is at the center of the nanoribbon ($x_v \approx 0$) at different transversal positions given by the carbon atom row number $N_v$. For results obtained varying the $x$-position at fixed $N_v$ see the main text. The purpose of this section is to provide a more complete picture of the vacancy effect on the optical response of the GNRs. This also allows to further illustrate the link between the transport of the optically excited charge carriers in presence of the vacancy and the effect of the latter on plasmonic modes of the nanoribbon. To this end the calculations were performed

- For different types of the nanoribbons: the metallic AGNR and the ZGNR showing different electronic properties and thus different vacancy effect on electron transport;
- For various levels of the electronic doping (expressed in terms of the Fermi $E_F$) allowing to change the energies of the electronic states relevant for the optical excitation;
- Varying the transverse position of the vacancy created close to the middle of the ribbon in longitudinal direction ($x_v \approx 0$), which allows to change the vacancy effect on the electron transport.

We start our discussion with results obtained for undoped metallic AGNR-11 and shown in Fig. S5a. For the transversal displacement of the vacancy among the $N_v = 1, 2, 4, 7, 8, 10, 11$ atomic rows of the nanoribbon we retrieve the results of the main text obtained for $N_v = 5$. Namely, the vacancy plays a role of an efficient reflector of the optically induced currents. Effectively, the nanoribbon is splitted in two parts forming plasmonic dimer, which results in the blue-shift of the $p = 1$ dipolar plasmon (DP) frequency. However, for $N_v = 3j,\ j = 1, 2, 3$ the vacancy has no effect on the plasmon resonance. In fact, because of the quantization of transversal electron motion, these carbon atom rows correspond to the nodal lines of the wave functions of the gapless subbands ($n = 0$) close to the Dirac point [25–27]. The vacancy placed at these atom rows does not reflect the corresponding electrons moving along the nanoribbon [27].

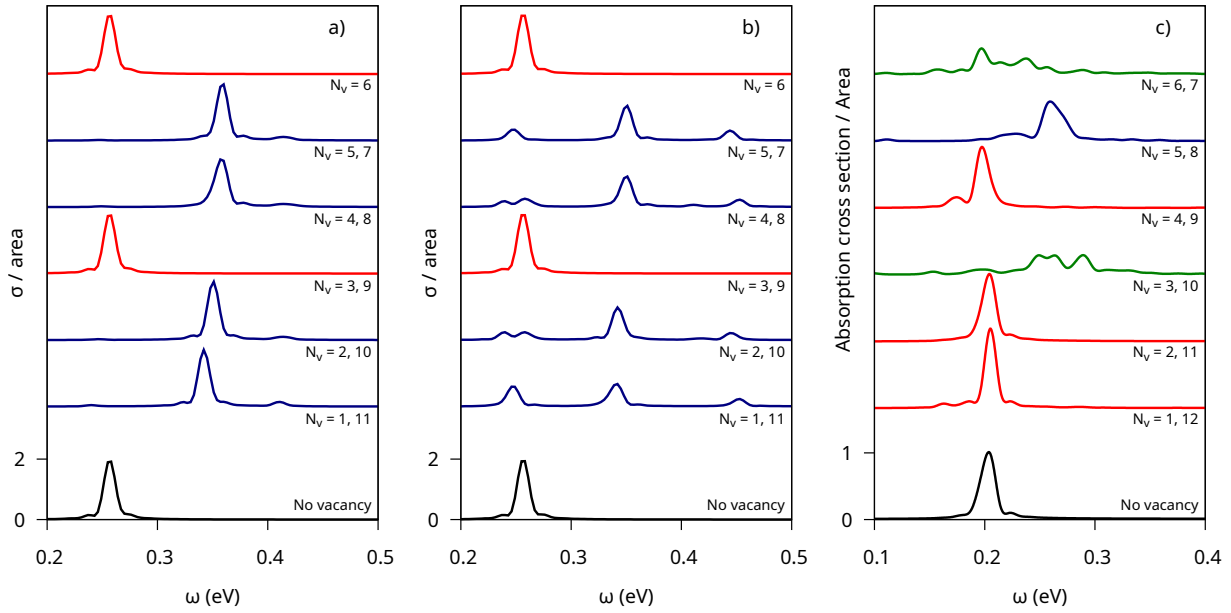


FIG. S5. Optical absorption cross section per area of metallic AGNR-11 and ZGNR-12. Results are shown as function of the frequency of the $x$-polarized electromagnetic plane wave. The situations with undoped AGNR-11 ($E_F = 0$, **panel a**), and AGNR-11 electronically doped to the Fermi energy $E_F = 0.4$ eV (**panel b**) are considered. The ZGNR-12 is electronically doped ($E_F = 0.4$ eV, **panel c**). The TDTB results obtained for ideal GNRs are shown with black curves, and the TDTB results obtained for the GNRs with single carbon atom vacancy are shown with color curves. The vacancy is created close to the middle of the ribbon in longitudinal direction ($x_v \approx 0$), and at different carbon atom rows $N_v$, as indicated for each data set. Different colors allow to distinguish main trends (reflector-blue, quencher-green, and idler-red) depending on the lateral position of the vacancy. An artificial broadening $\gamma = 5$ meV has been applied.

With an electron doping up to $E_F = 0.4$ eV (Fig. S5b), the AGNR-11 is still transverse monomode, at least for the electronic states within the energy range studied here (see Fig. S4). Nevertheless, the optically excited electrons have different (overall higher) energy range, where the effective reflectivity of the vacancy features the energy dependence [27, 28]. Indeed, for the excitation frequency $\omega \approx 0.25$ eV the reflectivity of the vacancy is not as efficient as in the $E_F = 0$ case, while it is high for $\omega \approx 0.35$ eV. This is clearly witnessed by the DP spectrum obtained with a vacancy on row $N_v = 1$ (or $N_v = 11$), which presents one peak at $\omega \approx 0.34$ eV associated with formation of the dimer, together with a broad peak at $\omega \approx 0.25$ eV associated with a broadened dipolar plasmon of the AGNR-11 nanoribbon.

The ZGNR-12 (Fig. S5b) also shows the clear dependence of the optical response on the transversal vacancy position $N$. In turn, this can be linked with the dependence of the electron reflectivity of the vacancy defect on the position of the later [28–31]. The vacancy created close to the edges of the nanoribon in the $N_v = 1, 2, 11, 12$ carbon atom rows has little effect on the electron scattering and thus on the plasmon modes. When the vacancy is located closer to the center, the situation is more involved. Various effects on the dipolar plasmon resonance are observed. For $N_v = 3, 6, 7, 10$, the resonant features in absorption spectrum are strongly broadened and quenched as discussed in the main text. For $N_v = 4, 9$ the vacancy does not produce any significant effect on the adsorption spectra. Finally for $N_v = 5, 8$ the vacancy behaves as a reflector and blue-shifts the dipolar plasmon resonance.

## TRANSITION TO THE WIDE RIBBON LIMIT

The results presented in the main text of the paper correspond to a width $W$ of the nanoribbon where the confinement of the electron motion in the transversal $y$-direction and its subsequent quantization is such that the single channel conducts the optically induced currents along the nanoribbon. That is the reason for the strong vacancy effect on the electron transport and optical response. Indeed, the energy bands corresponding to the quantized states in transversal direction with larger quantum numbers are unaccessible considering the frequency range of the plasmon modes $\omega \leq 1$ eV relevant for our study (see Fig. S4).

However, increasing the width of the nanoribbon, or electronically doping the nanoribbon to sufficiently high Fermi energy $E_F$ allows the optical excitation into these higher energy bands. This is because (i) with increasing $W$ the characteristic wavelength corresponding to the transversal confinement increases so that the energies of the quantized bands downshift closer to the Dirac point [25, 26, 32, 33]; and (ii) the optically excited electrons have energies up to $E_F + \omega$ eventually allowing to reach the electronic states associated with higher transversal energies. When several transversal conduction channels contribute to the optically excited currents, one would expect that the effect of the vacancy decreases. In very simple terms the electron transport in the system evolves from 1D to 2D. The vacancy scattering becomes a multichannel problem with inter-band transitions so that strong backward reflection which electronically decouples the nanoribbon in two parts becomes less probable. One would rather expect the broadening of the plasmon via dephasing and Landau damping associated with vacancy scattering [11–17].

In order to illustrate the effect of the width of the nanoribbon, we have performed the TDTB calculations of the optical absorption cross section of the metallic AGNRs (the number of carbon atom rows $N = 3\ell + 2, \ell = 1, 2, \dots$), and of the ZGNRs of variable thickness. The nanoribbons are electronically doped to the Fermi energy $E_F = 0.4$ eV, as measured with respect to the Dirac point ($E_F = 0$ corresponds thus to the undoped nanoribbon). We considered the $x$-polarised electromagnetic plane wave incidence, and the frequency range characteristic for the dipolar plasmon of the nanoribbon. Results are shown in Fig. S6 For the narrow nanoribbon only the $n = 0$ bands (see Fig. S4) participate in the optical excitations. Depending on the type of the nanoribbon, and the transverse positions of the

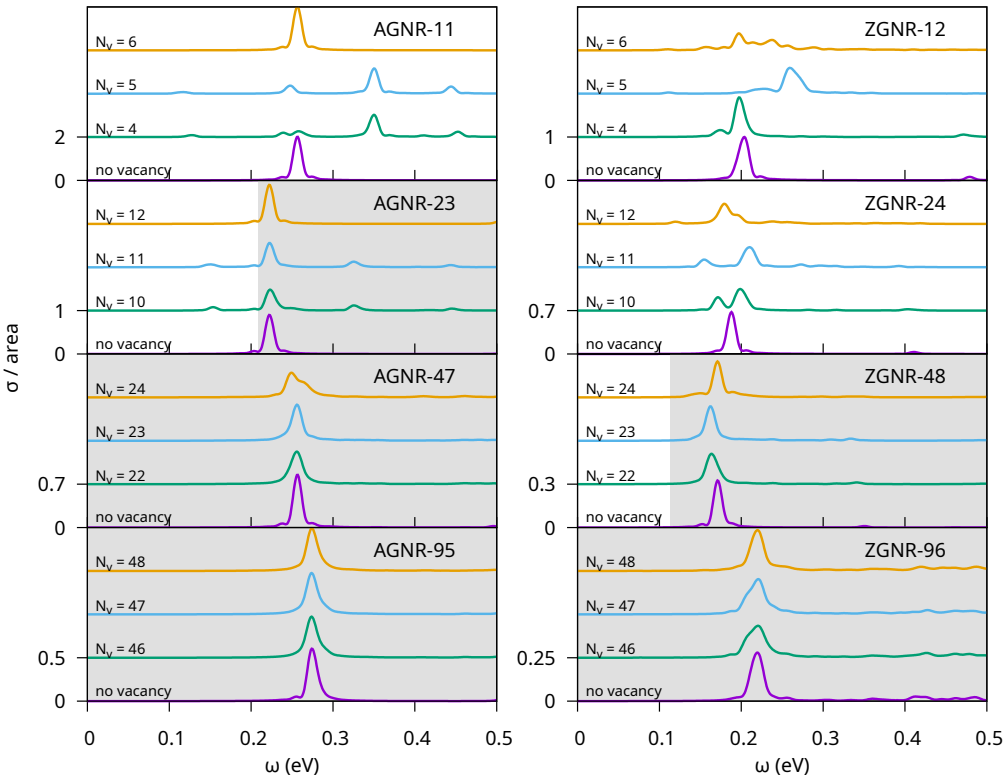


FIG. S6. The optical absorption cross section $\sigma$ of the GNRs normalized to their area. Results are shown as function of the frequency of an incident $x$-polarised electromagnetic plane wave. The vacancy is created at different carbon atom rows near the middle of the ribbon ($x_v \approx 0$). The index of the carbon atom row $N_v$ containing the vacancy is indicated for each data set in the panels of the figure. Results obtained with different $N_v$ are vertically offset for clarity. Each vertical set of panels corresponds to the same type of the nanoribbon (AGNR-$N$ or ZGNR-$N$), $N$ being the number of carbon atom rows. The nanoribbons are electronically doped to the Fermi energy $E_F = 0.4$ eV, as measured with respect to the Dirac point. The panels from the top to the bottom show the evolution of the absorption spectra with increasing width $W$ of the nanoribbon. The grey shaded areas corresponds to region where at least two electronic bands are energetically accessible during the photo-excitation, i.e. $\omega + E_F \geq E_{n=1}$. An artificial broadening $\gamma = 5$ meV has been applied.

vacancy given by atomic row number $N_v$, the DP mode may be unaffected, blue shifted, or broadened as discussed in the previous section. When the width of the nanoribbon $W$, and/or the frequency of the electromagnetic radiation $\omega$, is such that the $n = 1$ (see Fig. S4)

band becomes accessible for optical excitation, the vacancy effect is drastically reduced, and basically one retrieves the broadened plasmon of the $L$-long nanoparticle with no sensitivity to the transverse location of the vacancy.

* andrei.borissov@universite-paris-saclay.fr

[1] F. Aguillon, D. C. Marinica, and A. G. Borisov, Molecule detection with graphene dimer nanoantennas, The Journal of Physical Chemistry C **124**, 28210 (2020).

[2] S. Thongrattanasiri, A. Manjavacas, and F. J. García de Abajo, Quantum finite-size effects in graphene plasmons, ACS Nano **6**, 1766 (2012).

[3] J. D. Cox, I. Silveiro, and F. J. García de Abajo, Quantum effects in the nonlinear response of graphene plasmons, ACS Nano **10**, 1995 (2016).

[4] I. Silveiro, J. M. P. Ortega, and F. J. G. de Abajo, Quantum nonlocal effects in individual and interacting graphene nanoribbons, Light: Science and Applications **4**, e241 (2015).

[5] J. D. Cox and F. J. G. de Abajo, Transient nonlinear plasmonics in nanostructured graphene, Optica **5**, 429 (2018).

[6] J. D. Cox and F. J. García de Abajo, Nonlinear atom-plasmon interactions enabled by nanostructured graphene, Phys. Rev. Lett. **121**, 257403 (2018).

[7] C. Leforestier, R. H. Bisseling, C. Cerjan, M. D. Feit, R. Friesner, A. Guldberg, A. Hammerich, G. Jolicard, W. Karrlein, H. D. Meyer, N. Lipkin, O. Roncero, and R. Kosloff, A comparison of different propagation schemes for the time dependent schr¨dinger equation, Journal of Computational Physics **94**, 59 (1991).

[8] R. Carminati, A. Cazé, D. Cao, F. Peragut, V. Krachmalnicoff, R. Pierrat, and Y. De Wilde, Electromagnetic density of states in complex plasmonic systems, Surface Science Reports **70**, 1 (2015).

[9] L. Novotny and B. Hecht, *Principles of Nano-Optics* (Cambridge University Press, 2006).

[10] P. Bharadwaj, B. Deutsch, and L. Novotny, Optical antennas, Adv. Opt. Photon. **1**, 438 (2009).

[11] M. Jablan, H. Buljan, and M. Soljačić, Plasmonics in graphene at infrared frequencies, Phys. Rev. B **80**, 245435 (2009).

[12] T. Low and P. Avouris, Graphene plasmonics for terahertz to mid-infrared applications, ACS Nano **8**, 1086 (2014).

[13] T. Langer, J. Baringhaus, H. Pfnür, H. W. Schumacher, and C. Tegenkamp, Plasmon damping below the landau regime the role of defects in epitaxial graphene, New Journal of Physics **12**,

033017 (2010).

[14] H. Yan, T. Low, W. Zhu, Y. Wu, M. Freitag, X. Li, F. Guinea, P. Avouris, and F. Xia, Damping pathways of mid infrared plasmons in graphene nanostructures, Nature Photonics **7**, 394 (2013).

[15] C. Lewandowski and L. Levitov, Intrinsically undamped plasmon modes in narrow electron bands, Proceedings of the National Academy of Sciences **116**, 20869 (2019).

[16] V. N. Kotov, B. Uchoa, V. M. Pereira, F. Guinea, and A. H. Castro Neto, Electron-electron interactions in graphene: Current status and perspectives, Rev. Mod. Phys. **84**, 1067 (2012).

[17] F. Aguillon, D. C. Marinica, and A. G. Borisov, Plasmons in graphene nanostructures with point defects and impurities, The Journal of Physical Chemistry C **125**, 21503 (2021).

[18] F. Karimi and I. Knezevic, Plasmons in graphene nanoribbons, Phys. Rev. B **96**, 125417 (2017).

[19] D. Novko, Dopant induced plasmon decay in graphene, Nano Letters **17**, 6991 (2017), pMID: 28972379, https://doi.org/10.1021/acs.nanolett.7b03553.

[20] N. J. Halas, S. Lal, W.-S. Chang, S. Link, and P. Nordlander, Plasmons in strongly coupled metallic nanostructures, Chemical Reviews **111**, 3913 (2011).

[21] P. Nordlander, C. Oubre, E. Prodan, K. Li, and M. I. Stockman, Plasmon hybridization in nanoparticle dimers, Nano Letters **4**, 899 (2004).

[22] A. Y. Nikitin, T. Low, and L. Martin-Moreno, Anomalous reflection phase of graphene plasmons and its influence on resonators, Phys. Rev. B **90**, 041407 (2014).

[23] C. E. P. Villegas, M. R. S. Tavares, G.-Q. Hai, and P. Vasilopoulos, Plasmon modes and screening in double metallic armchair graphene nanoribbons, Phys. Rev. B **88**, 165426 (2013).

[24] L. Brey and H. A. Fertig, Elementary electronic excitations in graphene nanoribbons, Phys. Rev. B **75**, 125434 (2007).

[25] L. E. F. Foa Torres, S. Roche, and J.-C. Charlier, *Introduction to Graphene-Based Nanomaterials: From Electronic Structure to Quantum Transport*, 2nd ed. (Cambridge University Press, 2020) pp. 11–69.

[26] K. Wakabayashi, K. ichi Sasaki, T. Nakanishi, and T. Enoki, Electronic states of graphene nanoribbons and analytical solutions, Science and Technology of Advanced Materials **11**, 054504 (2010).

[27] H.-Y. Deng and K. Wakabayashi, Vacancy effects on electronic and transport properties of

graphene nanoribbons, Phys. Rev. B **91**, 035425 (2015).

[28] T. C. Li and S.-P. Lu, Quantum conductance of graphene nanoribbons with edge defects, Phys. Rev. B **77**, 085408 (2008).

[29] N. Gorjizadeh, A. A. Farajian, and Y. Kawazoe, The effects of defects on the conductance of graphene nanoribbons, Nanotechnology **20**, 015201 (2008).

[30] D. A. Bahamon, A. L. C. Pereira, and P. A. Schulz, Tunable resonances due to vacancies in graphene nanoribbons, Phys. Rev. B **82**, 165438 (2010).

[31] Z. Kan, M. Khatun, and A. Cancio, Quantum transport in zigzag graphene nanoribbons in the presence of vacancies, Journal of Applied Physics **125**, 164305 (2019).

[32] Y.-W. Son, M. L. Cohen, and S. G. Louie, Energy gaps in graphene nanoribbons, Phys. Rev. Lett. **97**, 216803 (2006).

[33] L. Brey and H. A. Fertig, Electronic states of graphene nanoribbons studied with the dirac equation, Phys. Rev. B **73**, 235411 (2006).